Tuning Dynamically Formed Active Phases and Catalytic Mechanisms of *in Situ* Electrochemically-Activated Layered Double Hydroxide for Oxygen Evolution Reaction

Soressa Abera Chala,[a,c] Meng-Che Tsai,*[b,c] Bizualem Wakuma Olbasa,[a,c] Keseven Lakshmanan,[b,c] Wei-Hsiang Huang,[b,c,e] Wei-Nien Su,*[b,c] Yen-Fa Liao,[e] Jyh-Fu Lee,[e] Hongjie Dai,[d] Bing Joe Hwang*[a,b,c,e]

[a] *NanoElectrochemistry Laboratory, Department of Chemical Engineering, National Taiwan University of Science and Technology, Taipei 106, Taiwan.*

[b]*NanoElectrochemistry Laboratory, Graduate Institute of Applied Science and Technology, National Taiwan University of Science and Technology, Taipei 10607, Taiwan*

[c]*Sustainable Energy Development Center, National Taiwan University of Science and Technology, Taipei 106, Taiwan*

[d]*Department of Chemistry, Stanford University, Stanford, California 94305, United States*

[e] *National Synchrotron Radiation Research Center, Hsin-Chu, 30076, Taiwan*

[*]*Corresponding Authors: E-mail: bjh@mail.ntust.edu.tw (BJ Hwang); wsu@mail.ntust.edu.tw (WN Su); and mctsai@mail.ntust.edu.tw (MC Tsai)*

Experimental Section

Turnover Frequency (TOF). TOF was calculated according to the following equation.

$$\mathrm{TOF} = \frac{J \cdot A}{4 \cdot F \cdot n} \quad \text{(S1)}$$

where *J* is the measured current density at an overpotential of 300 mV, A is the surface area of the electrode, number 4 represents four-electron transfer for per mole of O_2, F is the Faraday constant, and n is the number of moles of the Ni atom loaded on the electrode.

The in situ Raman Measurements. The Raman measurements were implemented in a confocal UniRAM micro-Raman spectroscopy integrated by Protrustech Co., Ltd using thermoelectrically cooled charge-coupled (CCD) working at −60 °C and 50x objective in a backscattering geometry with the excitation source of laser wavelength of 633 nm. The electrochemical-Raman measurements were performed with a potentiostat (PGSTAT302N, Metrohm Autolab), using a homemade three-electrode system Ag/AgCl (sat. KCl, sat. AgCl), platinum, and modified glassy carbon electrode (GCE) were used as a reference, counter electrode, and working electrode, respectively. The electrochemical-Raman measurements were made in the aqueous solution of 0.1 M KOH electrolyte before and after the guest anions (13 mM chloride and bromide) were introduced into the electrolyte. The measurements were executed chronoamperometrically. All potentials for these measurements are reported *versus* the reversible hydrogen electrode (RHE).

In situ X-ray Absorption Spectroscopy. X-ray absorption spectra (XAS) were recorded at the beamline BL12B1 of the Super Photon ring-8 GeV (Spring-8) and 17C1 of the National Synchrotron Radiation Research Centre (NSRRC) of Taiwan, following a procedure described in detail elsewhere.[1] The X-ray beam energy was regulated by a monochromator operating in fixed-exit mode using a Si (111)

crystal pair. The *in situ* X-ray absorption spectra, including X-ray Absorption Near Edge Fine Structure (XANES) and Extended X-ray Absorption Fine Structure (EXAFS), were collected for the Ni K-edge and Mn K-edge using transmission mode. The *in situ* measurement was performed in 0.1 M KOH at the various applied potential within a potential range of oxygen evolution reaction (OER) at room temperature with (13 mM of Br^-) and without the guest anion. The spectra were collected after applying a potential for at least 20 minutes to ensure that the system had reached a steady-state in each condition. Prior to XAS measurement, the NiMn-LDH/carbon paper (CP) electrodes were prepared by dropping catalyst ink. In general, the amounts of Ni and Mn on the CP electrode were controlled to reach the edge jump of Ni around 1~1.5 and ensured enough amount for Mn in the transmission mode measurement. A schematic of the *in situ* setup is shown in **Figure S1**. The control of parameters for EXAFS measurements, data collection modes, and calculation of errors were all done as per the guidelines set by the International XAFS Society Standards and Criteria Committee. Standard procedures were followed to analyze the XAS data. First, the raw absorption spectrum in the pre-edge region was fitted to a straight line, while the background above the edge was fitted with a cubic spline. The EXAFS function, χ, was obtained by subtracting the post-edge background from the overall absorption and then normalized with respect to the edge jump step. The normalized $\chi(E)$ was transformed from energy space to *k*-space, where *k* is the photoelectron wave vector. The $\chi(k)$ data were multiplied by k^2 or k^3 to compensate for the damping of EXAFS oscillations in the high *k*-region. Subsequently, k^2- or k^3-weighted $\chi(k)$ data in the k-space ranging from 3.6 to 11.4 $Å^{-1}$ for Ni K-edge and from 3.1 to 10.3 $Å^{-1}$ for Mn K-edge were Fourier transformed (FT) to *r*-space to separate the EXAFS contributions from the different coordination shells. A nonlinear least-squares algorithm was applied to the curve fitting of the EXAFS in the *r*-space between 0.8 and 3.2 Å for Ni K-edge. Due to the possible presence

of two structure phases at the applied potential, the models of $Ni(OH)_2$ and NiOOH are used to perform EXAFS fitting for some conditions. All of the computer programs were implemented in the Athena 0.8.056 package with the backscattering amplitude and the phase shift for the specific atom pairs being theoretically calculated by using Ifeffit 1.2.11 code. From these analyses, structural parameters, such as coordination number (N), bond distance (R), the Debye-Waller factor ($\Delta\sigma^2$), and the inner potential shift (ΔE_0), were calculated.

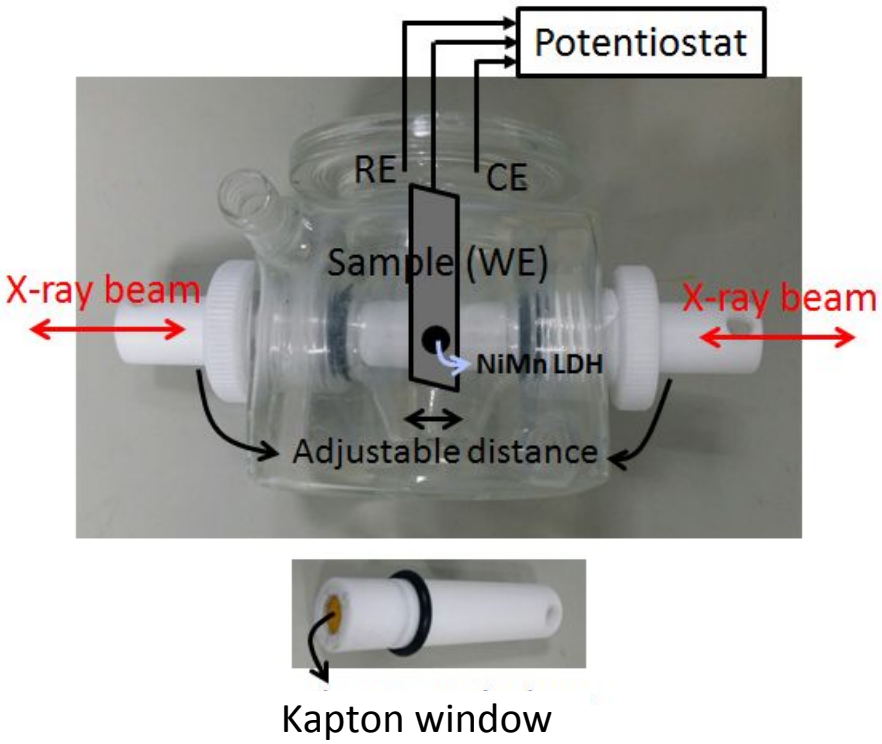

Figure S1. A photograph of *in situ* XAS setup for transmission mode. One side of the Teflon tubes is sealed by Kapton tapes to avoid leakage of the electrolyte during the test. The space nearby working electrode is adjustable by two Teflon tubes to ensure enough contact between electrode and electrolyte under applied potential. During spectra collection, the distance can be decreased to lower than 1 mm to minimize the effect of liquid to X-ray penetration. WE, RE, and CE stand for working, reference, and counter electrodes.

Operando X-ray diffraction. The *in situ* XRD measurements were performed at the beamline of 01C1 of the NSRRC, Hsinchu, Taiwan, equipped with a gold target X-ray radiation (λ = 0.83 Å). The 2θ scan was implemented in the range of 5–100 degrees and then converted to Cu Kα_1 (1.5418 Å) to simplify the comparison with the reported literature and in-house XRD results. The electron storage ring was operated at 15 keV with a beam current of 360 mA. The *in situ* XRD patterns were collected using a homemade *in situ* cell upon potentiostatic cycling electrolyte (0.1 M KOH) before and after the guest anion (13 mM) introduced into the electrolyte. The diffraction patterns of each sample were collected at time intervals of 10 min for various applied potentials.

Computational details

All DFT calculations in the present work were performed by the Vienna *Ab initio* Simulation Package (VASP) 5.4.4 code[2] with the Perdew-Burke-Ernzerhof (PBE) functional.[3] The ion-electron interaction was described by the projector augmented wave (PAW) method[4] with a kinetic energy cutoff of 600 eV. A 2 × 2 × 2 supercell of the $Ni(OH)_2$ structure was employed to simulate the NiMn layered double hydroxide (NiMn-LDHs) with Ni/Mn atomic ratio of 3. A Monkhorst-Pack *k*-point mesh with a size of 5 × 5 × 3 was applied for the calculations. Considering the magnetic nature of Ni-based hydroxides, the spin polarization was employed for all calculations. In addition, the DFT-D3 correction method in Grimme's scheme[5, 6] was also used to accurately describe the long-range vdW interactions. For structural optimization, the atomic positions were allowed to relax in all three directions, while the shape and volume of the supercell were also relaxed until the total energy and force were less than 10^{-5} eV per atom and 0.05 eV $Å^{-1}$, respectively.

In order to be consistent with the experimentally prepared material, carbonate group (CO_3) as a host anion was located upon Mn sites of the NiMn-LDHs to reach charge compensation. The bulk model of NiMn-LDHs with host anion CO_3^{2-} is shown in **Figure S16a**. Due to the charge state of 2^- for the carbonate group, the total charge should be compensated by two LDHs (two Mn^{3+}) and one CO_3 group. Here the *d*-spacing along (001) direction of LDH layers was examined for CO3 or Br as the host anion and the cases with/without guest anion (Br), all the relaxed structures can be observed in **Figure S16a-c**. In addition, we also examine the ionic exchange between CO_3 and Br as the host anions. According to the calculation of the formation energy of reaction R1, thermodynamic feasibility for the ionic exchange between CO3 (Model A) and Br (Model B) in the LDH can be determined.

$$\text{NiMn-LDH-}CO_3^{2-} + 2\text{NaBr} \rightarrow \text{NiMn-LDH - }2Br^- + Na_2CO_3 \quad \text{(S2)}$$

Furthermore, the intercalation energy for the host/guest anion Br can be calculated to understand the effect of bromide, the energy calculation using the following equation (S2).

Considering Br^- as a host anion:

$$\Delta E_{int} = E_{LDH(2Br)} + E_{Na_2CO_3} - \left(E_{LDH(CO_3)} + 2E_{NaBr}\right) \quad \text{(S3)}$$

Considering Br^- as a guest anion:

$$\Delta E_{int} = E_{LDH(CO_3)+Br} - \left(E_{LDH(CO_3)} + \frac{1}{2}E_{Br_2}\right) \quad \text{(S4)}$$

Where $E_{LDH(CO_3)}$ is the total energy of NiMn-LDHs (Model A), $E_{LDH(2Br)}$ is the total energy of NiMn-LDHs (Model B), $E_{LDH(CO_3)+Br}$ is the total energy of Br-intercalated NiMn-LDHs (Model C), $E_{Na_2CO_3}$ is the total energy of Na_2CO_3 molecule, E_{NaBr} is the total energy of NaBr molecule andE_{Br_2} is the total energy of Br_2 molecule.

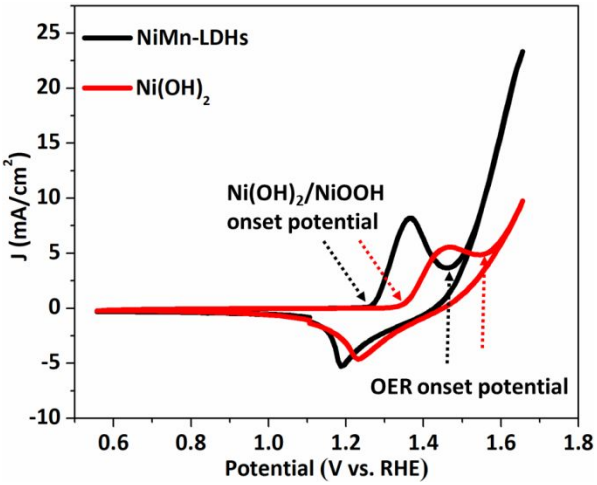

Figure S2. Cyclic voltammetry (CV) of NiMn-LDHs (black) and β-$Ni(OH)_2$ (red) in 1M KOH at 50 mV/s sweep rate.

It can be seen that the onset potential of $Ni(OH)_2$/NiOOH redox transition for LDHs slightly shifts to lower overpotential upon the introduction of guest anions, suggesting that the *in situ* intercalation of the guest anions offers higher site activity thereby boosted the OER activity. As more guest anions (1-7 mM) are introduced, the redox couple of $Ni(OH)_2$/NiOOH for NiMn-LDHs shifts to lower overpotentials, and the peak area of the redox couple increases (**Figure S3** and **Figure S4**).

Unlike the bromide guest anions, the peak area of the redox transition of $Ni(OH)_2$/NiOOH and its normalized current density is not significant as the concentration of Cl^- increased, as shown in **Figure S4**. In addition, the OER limiting current density of β-$Ni(OH)_2$ considerably decreased as the concentration of guest anions increased, demonstrating that the Ni sites were embedded with the anions finally led to descent site populations and accumulation structure of the material, which seriously affect the final OER activity. The inset of **Figure S3** and **Figure S4** shows the redox

transition of $Ni(OH)_2$/NiOOH species preceding the oxygen evolution, which is commonly found in Ni-based OER catalysts.[7-9]

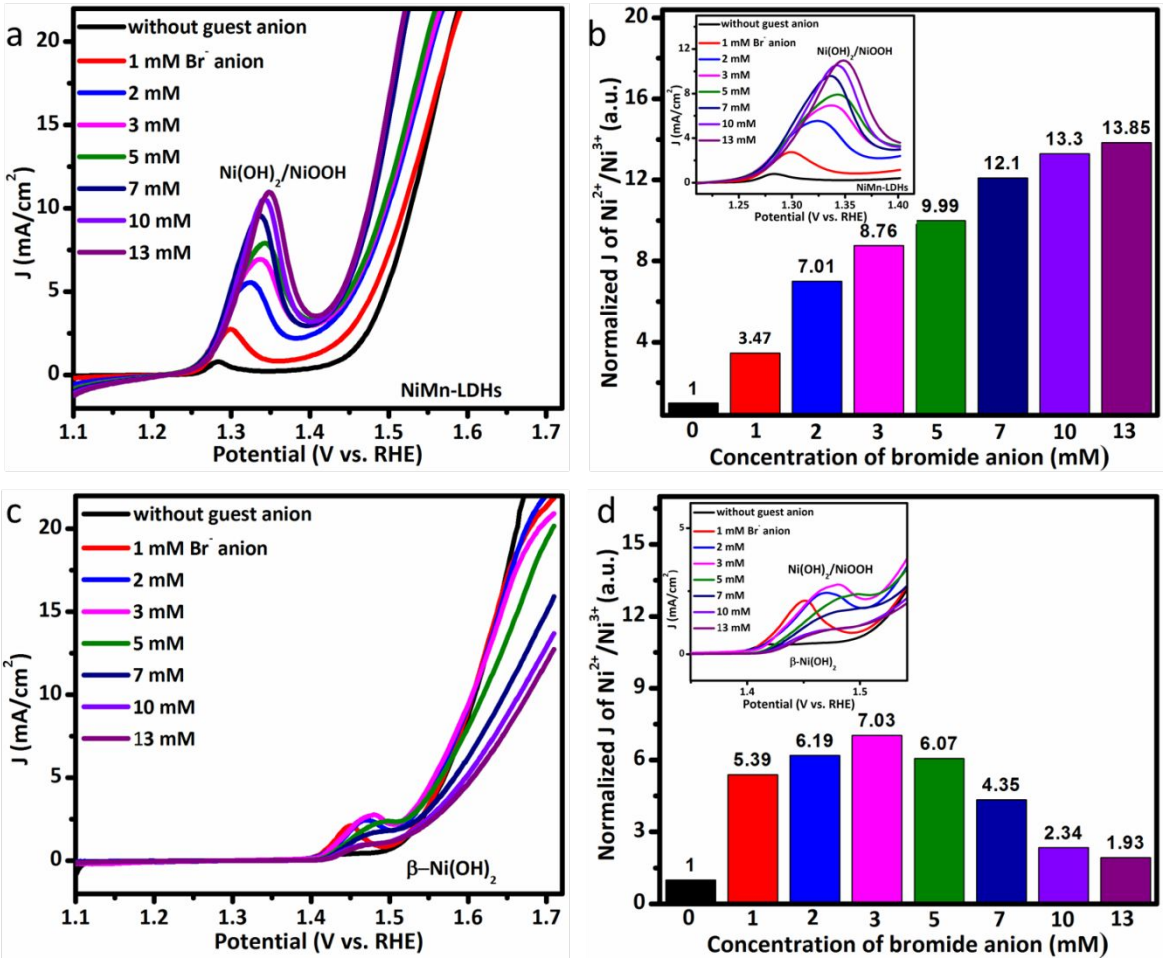

Figure S3. (a) OER LSV curves of NiMn-LDHs in the absence and presence of bromide (1-13 mM) guest anions in Ar-saturated 1M KOH at 1 mV/s sweep rate and rotation rate of 1600 rpm. (b) The normalized current density of the anodic $Ni(OH)_2$/NiOOH redox transitions of NiMn-LDHs at different concentration of bromide guest anions with respect to the current density obtained without the guest anions. (c) OER LSV curves of β-$Ni(OH)_2$ without and with bromide (1-13 mM) guest anions in Ar-saturated 1M KOH at 1 mV/s sweep rate and rotation rate of 1600 rpm. (d) The normalized current density of the anodic $Ni(OH)_2$/NiOOH redox transitions of β-

$Ni(OH)_2$. The inset is enlarged scale of redox transition of $Ni(OH)_2$/NiOOH for NiMn-LDHs and β-$Ni(OH)_2$ electrodes.

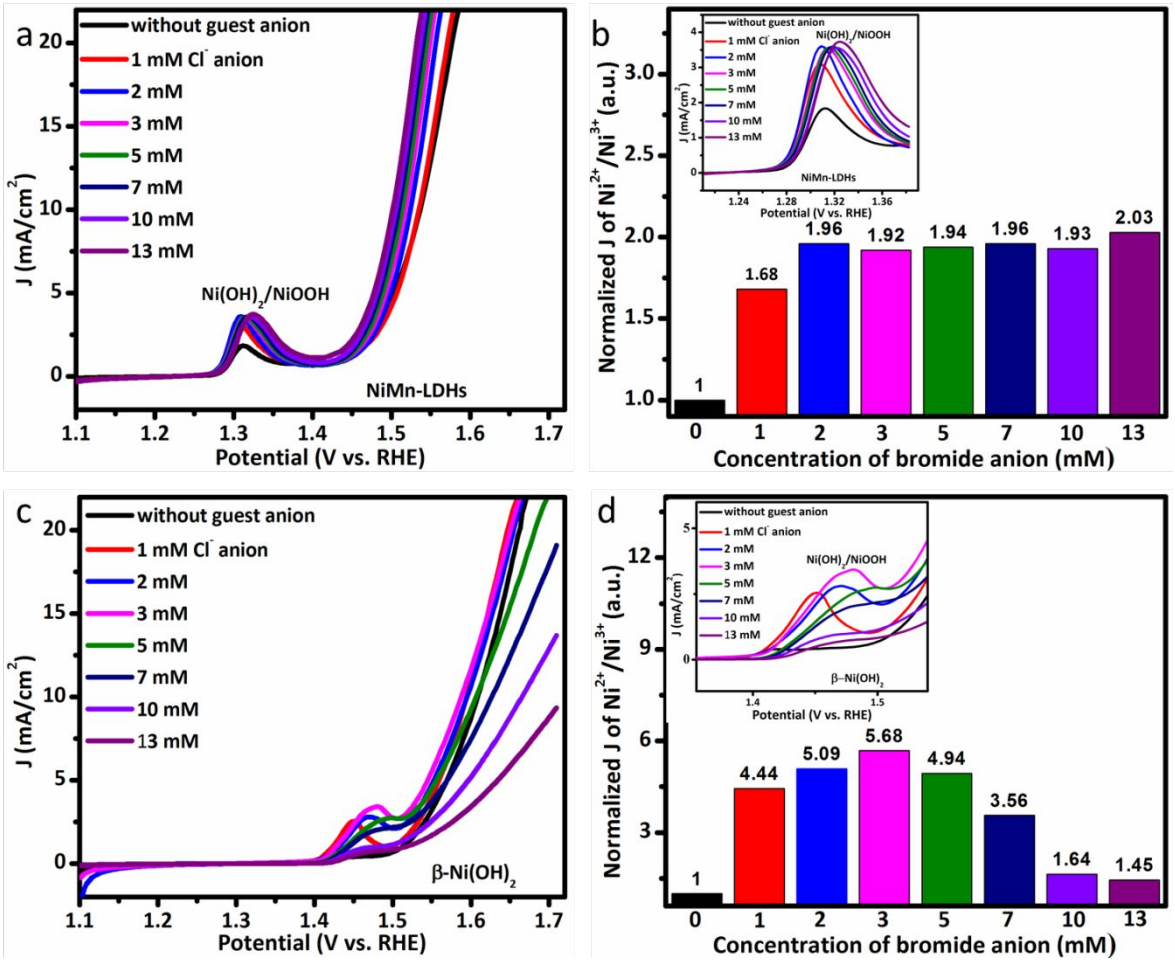

Figure S4. (a) OER LSV curves of NiMn-LDHs in the absence and presence of chloride (1-13 mM) guest anions in Ar-saturated 1M KOH at 1 mV/s sweep rate and rotation rate of 1600 rpm. (b) The normalized current density of the anodic $Ni(OH)_2$/NiOOH redox transitions of NiMn-LDHs at different concentrations of chloride guest anions with respect to the current density obtained without the guest anions. (c) OER LSV curves of β-$Ni(OH)_2$ in the absence and presence of chloride (1-13 mM) guest anions in Ar-saturated 1M KOH at 1 mV/s sweep rate and rotation rate of 1600 rpm. (d) The normalized current density of the anodic $Ni(OH)_2$/NiOOH redox

transitions of β-Ni(OH)$_2$. The inset is an enlarged scale of redox transition of Ni(OH)$_2$/NiOOH for NiMn-LDHs and β-Ni(OH)$_2$ electrodes.

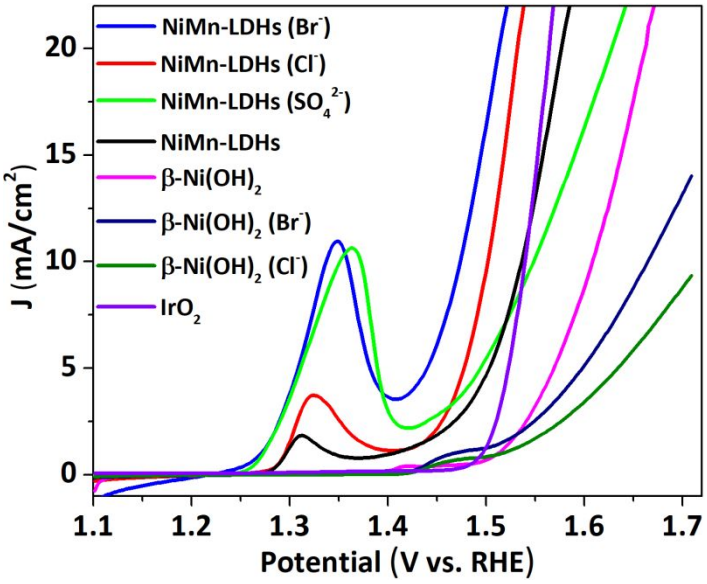

Figure S5. LSV curves of OER activity for NiMn-LDHs and β-N-(OH)$_2$ catalysts with and without guest anions evaluated in 1 M KOH at rotating speed of 1600 rpm along with the commercial IrO_2.

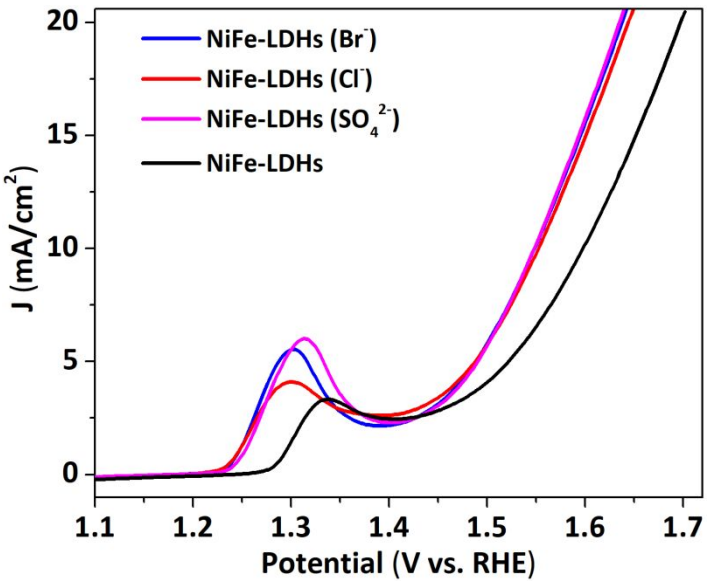

Figure S6. OER LSV curves of NiFe-LDHs with and without the guest anions in Ar-saturated 1 M KOH electrolytes with a scan rate of 1 mV s^{-1} and rotating speed of 1600 rpm.

The electrochemical active surface area (ECSA) is a crucial parameter to evaluate the relative performance.[10] To estimate the ECSA of NiMn-LDHs with and without the guest anions, CV tests are performed in a potential window of the non-faradaic region (0.90 – 1.20 V *vs*. RHE) at different scan rates (10 – 50 mV s^{-1}) in 1M KOH electrolyte. Next, the differences in current density variation ($\Delta J = J_a - J_c$) at 1.05 V *vs*. RHE are to be plotted against the scan rates. The plotted lines can be fitted by linear regression enabling the estimation of double-layer capacitance (C_{dl}), where the slope is twice of C_{dl}. The large C_{dl} manifests more exposed surface site populations.[11]

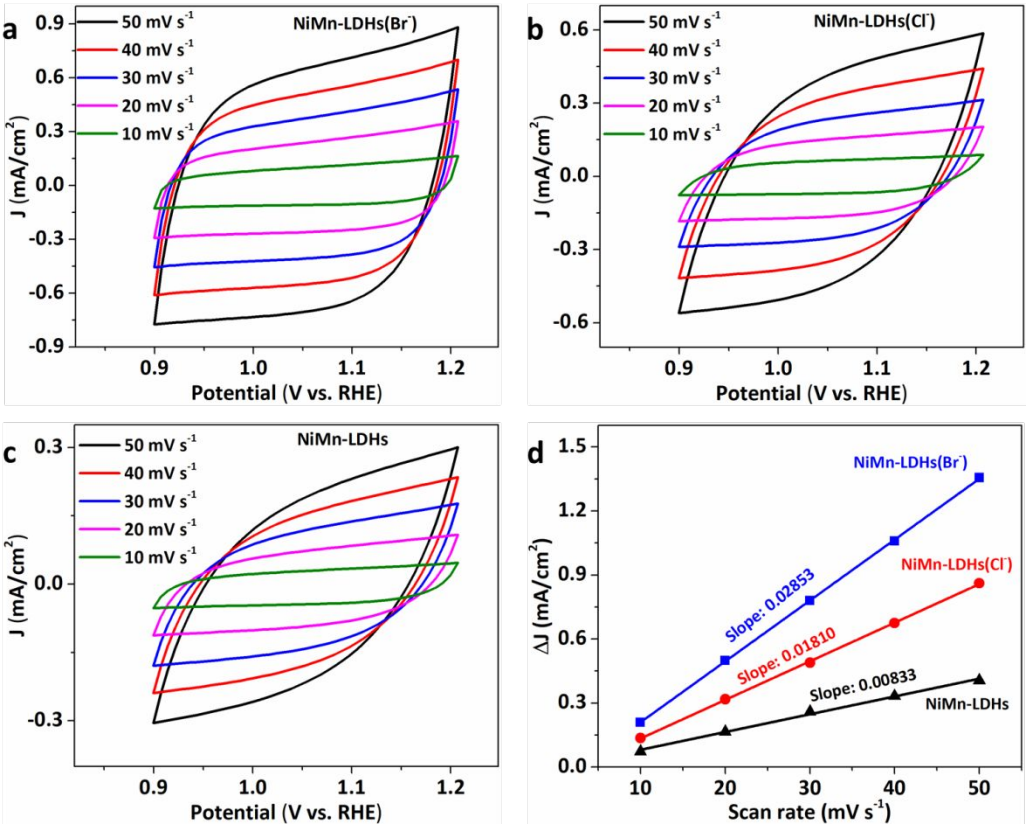

Figure S7. Cyclic voltammetry curves of (a) NiMn-LDHs (Br^-) (b) NiMn-LDHs (Cl^-) and (c) pristine NiMn-LDHs electrodes in 1M KOH with different scan rates; (d) $\Delta J = (J_a - J_c)$ of NiMn-LDHs (Br^-), NiMn-LDHs (Cl^-), and pristine NiMn-LDHs plotted against scan rates. The slopes equivalent to twice the double layer capacitance ($2C_{dl}$) were used to represent electrochemical active surface area (ECSA). The unit of slopes ($2C_{dl}$) is mF cm^{-2}.

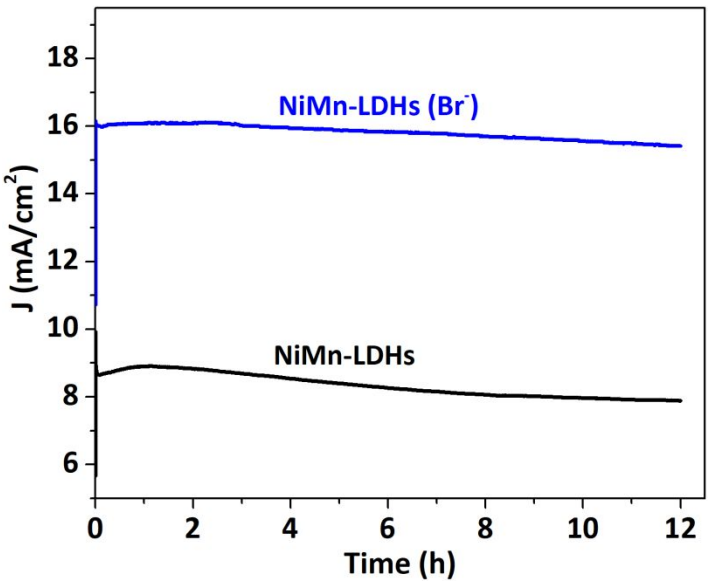

Figure S8. Chronoamperometric measurements of pristine NiMn-LDHs and NiMn-LDHs with Br^- guest at an overpotential of 270 mV for 12 h in 1M KOH electrolyte.

The gaseous products from the OER catalyzed by NiMn-LDHs with and without guest anions and commercial IrO_2 catalysts were analyzed using gas chromatography (GC). A constant overpotential of 270 mV was maintained for 3 h during gas chromatography measurement. Faradaic efficiency is estimated from the total amount of charge Q(C) passed through the cell and the total amount of produced oxygen n_{O2} (mol). Assuming that four electrons are needed to produce one O_2 molecule, the Faradaic efficiency can be calculated as follows:

Faradaic efficiency = $(4 \times n_{O2} \times F)/Q$

where F is the Faraday constant (96485 C/mol).

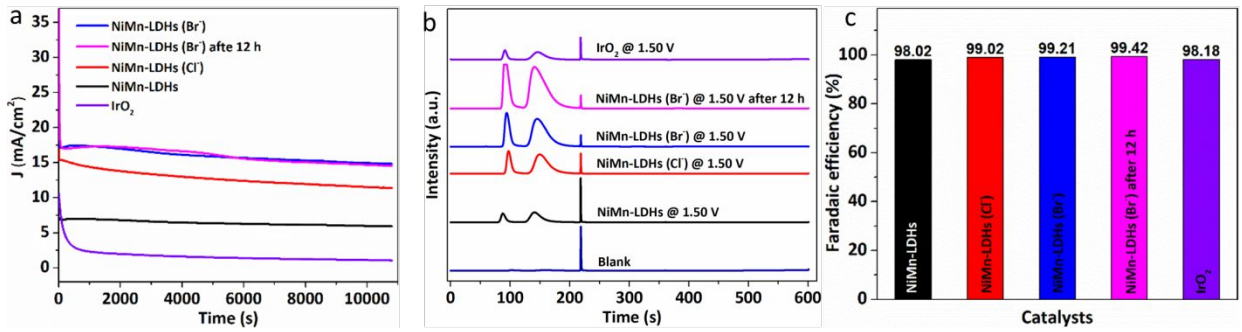

Figure S9. (a) Chronoamperometry curves of NiMn-LDHs with and without the guest anions and commercial IrO_2 catalysts at an overptential of 270 mV in Ar-saturated 1M KOH electrolyte during GC measurement. (b) GC curves (c) Faradaic efficiency of OER catalyzed by NiMn-LDHs with and without the guest anions and commercial IrO_2 electrodes at an overpotential of 270 mV. O_2 peak position were assigned by standard gas reference.

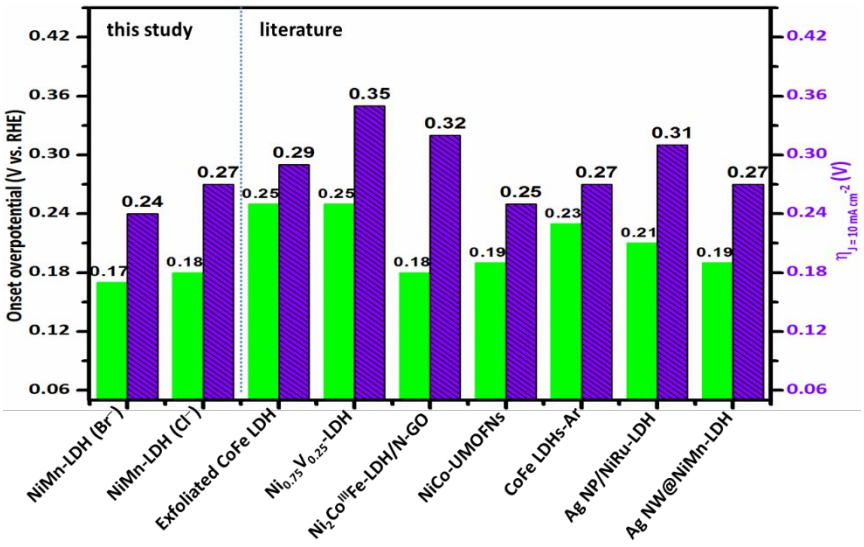

Figure S10. The OER onset overpotential and overpotentials required to deliver a current density of 10 mA/cm^2 for NiMn-LDH (with guest anions) catalysts of this study (left side) in comparison to the published literature (right side). Detailed activity values are given in **Table S1**.

Table S1. Comparison of the catalytic activity of *in situ* intercalated guest anions of NiMn-LDHs with the recently reported best electrocatalysts.

Electrocatalysts	Onset potential (V)	E_{OER} (V) (10 $mAcm^{-2}$)	OER Tafel slope ($mV\ dec^{-1}$)	Electrolyte KOH [M]	Reference
NiMn-LDHs (Br-)	1.40	1.47	29	1	This study
NiMn-LDHs (Cl-)	1.41	1.50	37	1	This study
Ag NW@NiMn-LDHs	1.42	1.50	40.2	1	[11]
Au/NiFe-LDHs	-	1.47	36	1	[12]
Ag NP/NiRu-LDHs	1.44	1.54	33	0.1	[7]
$Ni_2Co^{III}Fe$-LDH/N-GO	1.41	1.55	56.8	0.1	[13]
NiCo-UMOFNs	1.42	1.48	42	1	[14]
$Ni_{0.75}V_{0.25}$-LDHs	1.48	1.58	50	1	[10]
CoFe LDHs-Ar	1.46	1.50	37.85	1	[15]
H_2O-plasma exfoliated CoFe LDHs	1.48	1.52	27.8	1	[16]
NiFe-LDH/CNT	1.45	1.48 @ 5 $mAcm^{-2}$	31	1	[8]
3D NiFe-LDH-POM	-	1.43	67	0.1	[17]

As shown in **Figure S11a-b**, the introduction of guest anions into the electrolyte accomplished with the anion interaction, and this interaction allows *in situ* intercalation of the guest anions between the interlayer spaces of LDHs. The *in situ* intercalation of guest anions interrupts the hydrogen bonds and ionic bonds in the interlayers of LDHs, disturbing the normal charge balance and increases the interlayer spaces of LDH which leads to delamination of the positively charged host layers from each other. Thus, the *in situ* intercalation of the guest anions in the layers of LDHs can increase the interlayer spaces of the nanosheets which in turn affects the intrinsic properties of

the site activity and site populations thereby leads to high OER activity. Moreover, the introduction of guest anions can tune the electronic properties and structure of LDH nanosheets which in turn influences the intrinsic properties of the active sites. The intensity and peak positions of characteristic diffraction peaks for β-$Ni(OH)_2$ remains unchanged during the OER process (**Figure S11c-d**). The diffraction peaks at 21° are attributed to the carbon paper substrate.

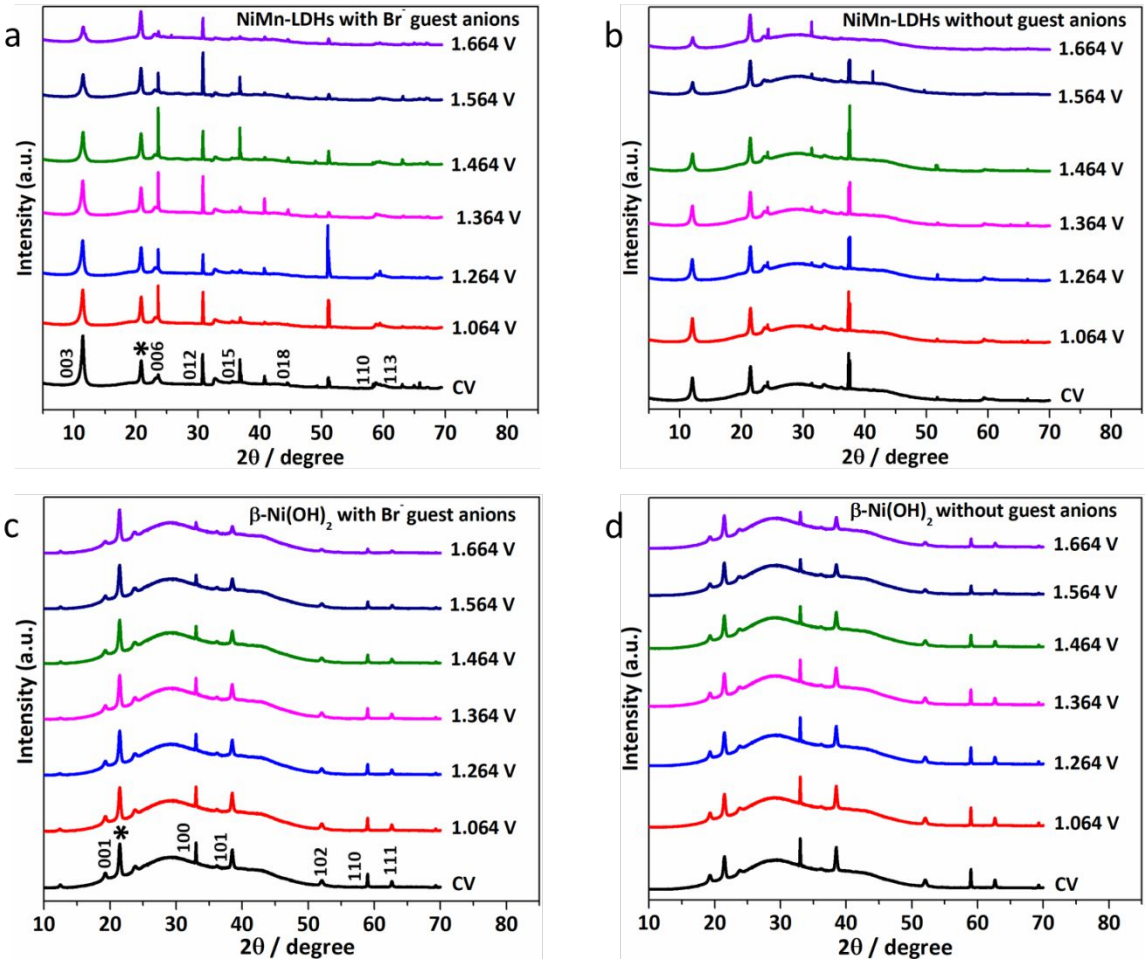

Figure S11. (a, b) *In situ* XRD patterns of NiMn-LDHs with and without Br^- guest anions during the OER process. (c, d) *In situ* XRD patterns of $Ni(OH)_2$ with and without guest anions during the OER process obtained at different potential chronoamperometrically.

It can be seen that the intensity of diffraction peak of 003 diffraction plane significantly decreases with increasing electrode voltage. The electrochemical result already confirmed that there is a reversible redox transition of $Ni(OH)_2$/NiOOH during the whole process of OER. However, there is no new peak detected due to the short lifetime of intermediate species (NiOOH) on the timescale of the XRD scans going on and thus keeps the diffraction peaks without any change.

Table S2. Basal spacing estimated from 003 and 006 diffraction patterns for the *in situ* XRD obtained during the OER process for NiMn-LDHs with and without Br^- guest anions.

	LDHs without anion				LDHs with guest anion			
Potential	003		006		003		006	
(V *vs.* RHE)	2θ	d-spacing (Å)	2θ	d-spacing (Å)	2θ	d-spacing (Å)	2θ	d-spacing (Å)
CV	12.043	7.340	24.242	3.666	11.443	7.724	23.600	3.765
1.064	12.043	7.340	24.243	3.666	11.421	7.739	23.607	3.764
1.264	12.021	7.353	24.250	3.665	11.422	7.738	23.615	3.763
1.364	12.043	7.340	24.257	3.664	11.421	7.739	23.622	3.762
1.464	12.085	7.314	24.257	3.664	11.471	7.705	23.615	3.763
1.564	12.085	7.314	24.279	3.661	11.471	7.705	23.615	3.763
1.646	12.113	7.297	24.343	3.652	11.471	7.705	23.643	3.759

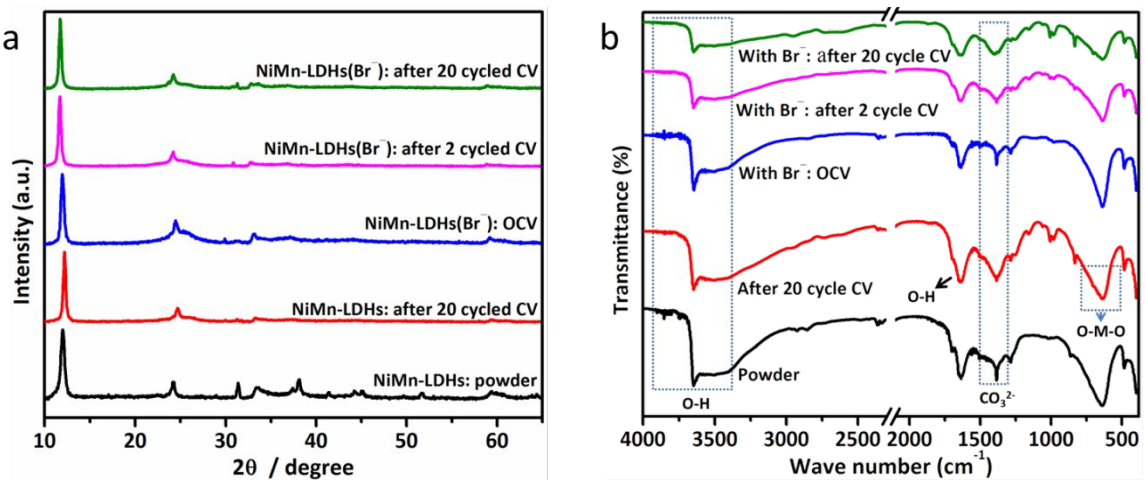

Figure S12. (a) XRD patterns and (b) FT-IR spectra of NiMn-LDHs before and after CV measurements with and without the guest anions.

Table S3. Basal spacing estimated from 003 and 006 diffraction patterns for the *ex situ* in-house XRD obtained before and after CV measurement for NiMn-LDHs with and without Br^- guest anions.

Samples	003		006	
	2θ	d-spacing	2θ	d-spacing
NiMn-LDHs: powder	12.00	7.37	24.25	3.66
NiMn-LDHs: after 20 cycle CV	12.21	7.24	24.71	3.60
NiMn-LDHs (Br^-): OCV	11.95	7.40	24.46	3.63
NiMn-LDHs (Br^-): after 2 cycle CV	11.71	7.55	24.22	3.67
NiMn-LDHs (Br^-): after 20 cycle CV	11.70	7.56	24.20	3.67

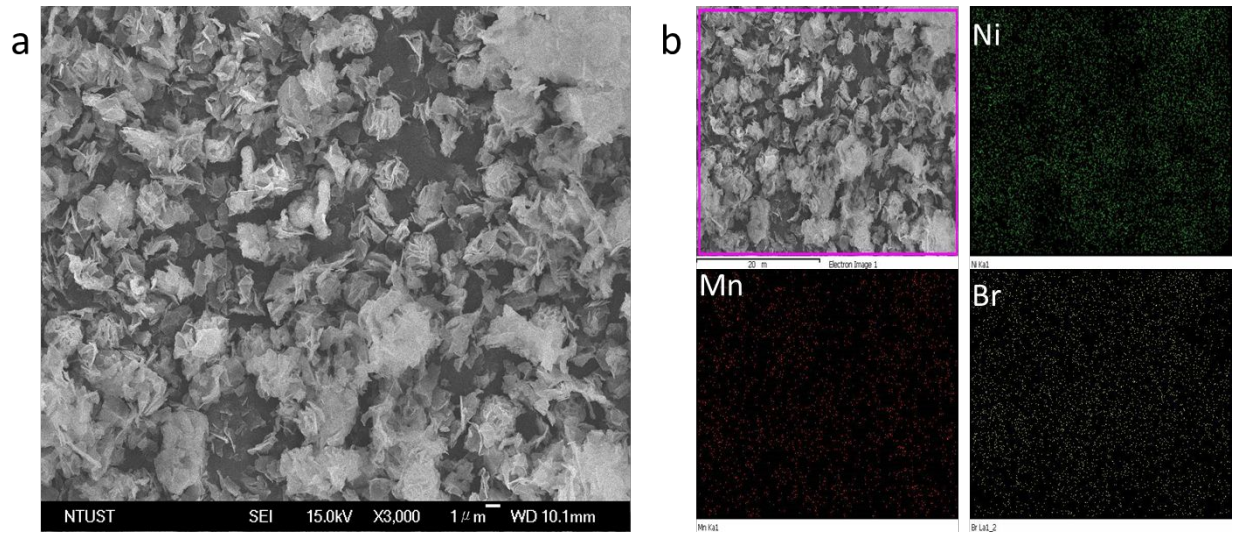

Figure S13. (a) The SEM image of NiMn-LDHs with guest anion (Br^-) after OCV and (b) the corresponding elemental distribution maps of Ni, Mn, and Br in the NiMn-LDHs electrode.

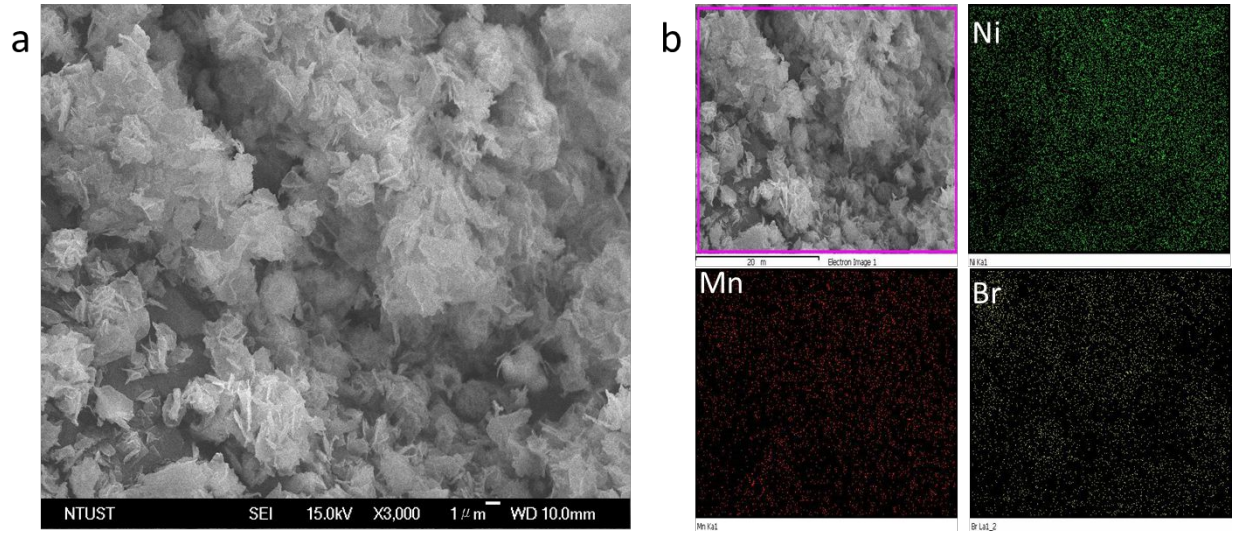

Figure S14. (a) The SEM image of NiMn-LDHs with guest anion (Br^-) after 2 cycled CV measurement and (b) the corresponding elemental distribution maps of Ni, Mn, and Br in the NiMn-LDHs electrode.

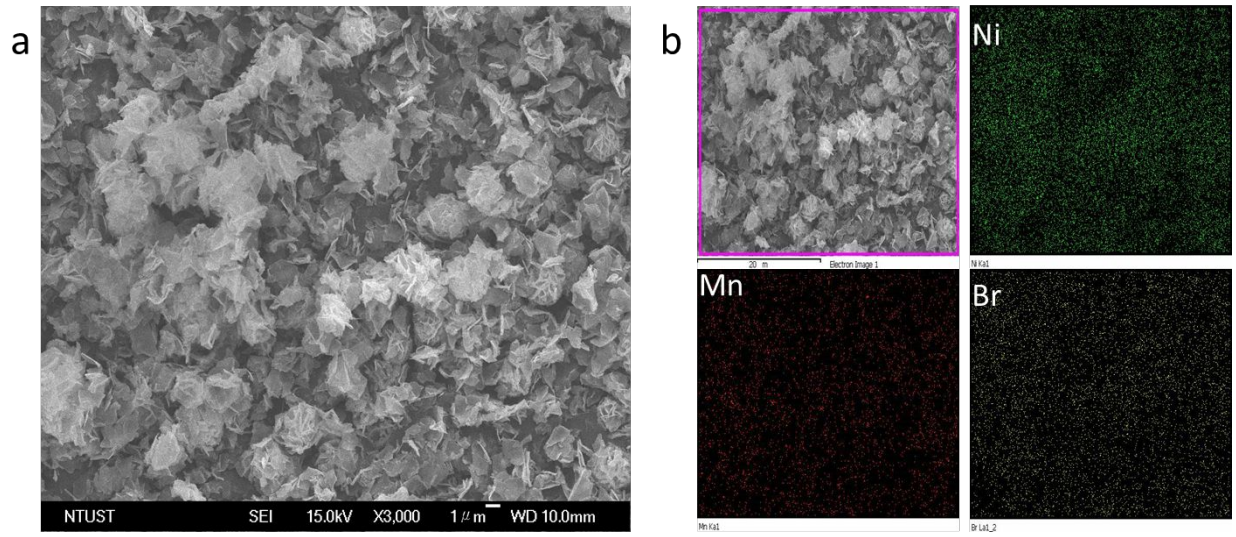

Figure S15. (a) The SEM image of NiMn-LDHs with guest anion (Br^-) after 20 cycled CV measurements and (b) the corresponding elemental distribution maps of Ni, Mn, and Br in the NiMn-LDHs electrode.

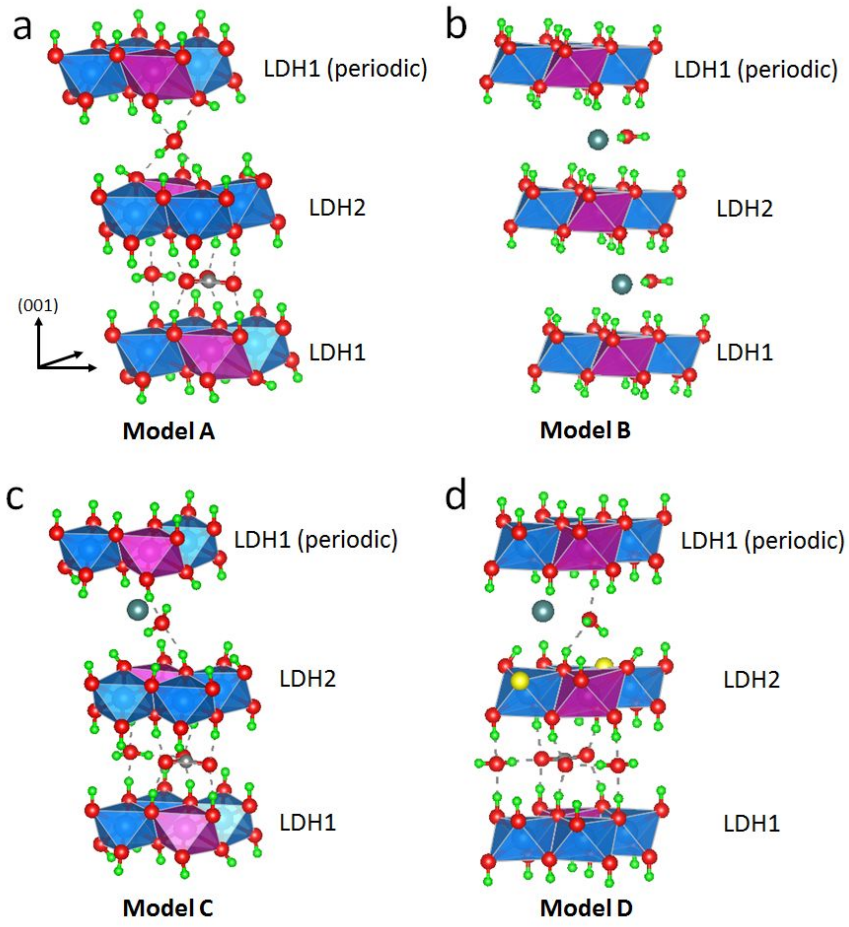

Figure S16. (a) A relaxed bulk model of NiMn-LDHs with intercalated CO_3 based on a 2 × 2 × 2 supercell of $Ni(OH)_2$ structure, denoted Model A. (b) A relaxed bulk model of two-layers NiMn-LDHs with two intercalated Br, denoted Model B. (c) A relaxed bulk model of NiMn-LDHs with a guest anion Br, where Br ion is located in the space between LDH2 and LDH1 (periodic), denoted Model C (d) A relaxed bulk model of NiMn-LDHs with one NiOOH site (yellow) and guest anion Br, created by removed one hydrogen on $Ni(OH)_2$ site, denoted Model D. Blue, purple, grey, red and green balls represent Ni, Mn, carbon, oxygen, and hydrogen, respectively.

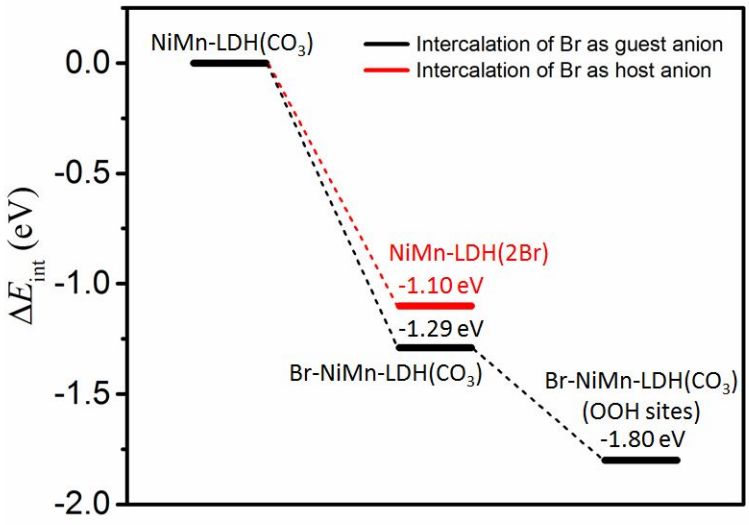

Figure S17. Energy profile of ΔE_{int} for Br as host anion (red) and guest anion (black) in NiMn-LDH. The calculations of ΔE_{int} are based on the total energy of NiMn-LDH(CO_3^{2-}).

Table S4. The calculated intercalation energy of intercalated CO_3^{2-} and Br^- anions in the NiMn-LDHs and *d*-spacing along the (001) direction in the NiMn-LDHs with different intercalated anions by DFT-D3 calculations.

Materials	Intercalated anion	ΔE_{int} / eV	d-spacing / Å
NiMn-LDHs	Host anion CO_3^{2-}(Model A)	N/A	6.9
	Host anion Br^- (Model B)	-1.10	7.8
	Guest anion Br^- (Model C)	-1.29	7.3
	Guest anion Br^- (Model D)	-1.80	7.1

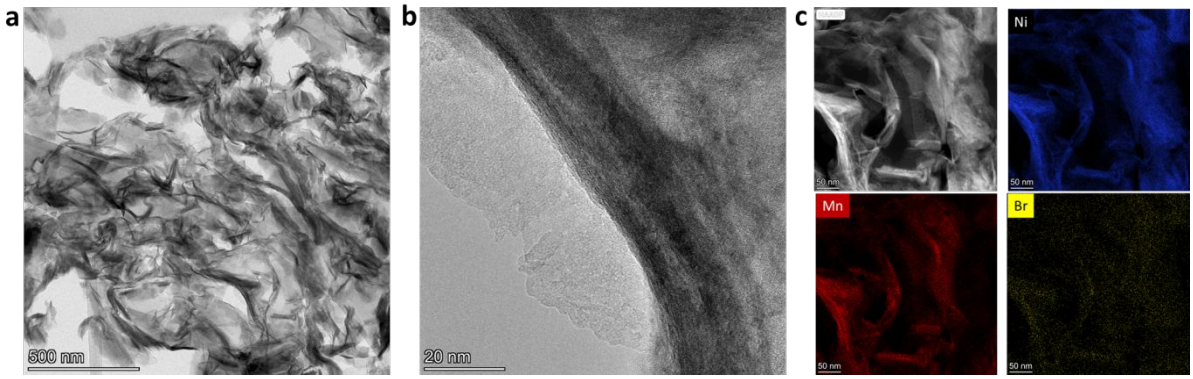

Figure S18. Characterization after the OER stability test. (a) TEM and (b) HRTEM (c) HAADF-STEM images of NiMn-LDHs with guest anions after the OER stability test at a constant overpotential of 270 mV in 1 M KOH solution 12 h and the corresponding EDS mapping.

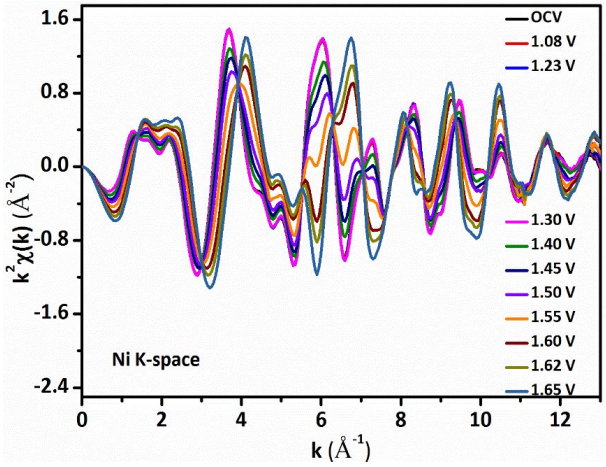

Figure S19. The *operando* XANES spectra of extended oscillation functions $k^2\chi(k)$ for Ni K-edge of NiMn-LDHs catalyst.

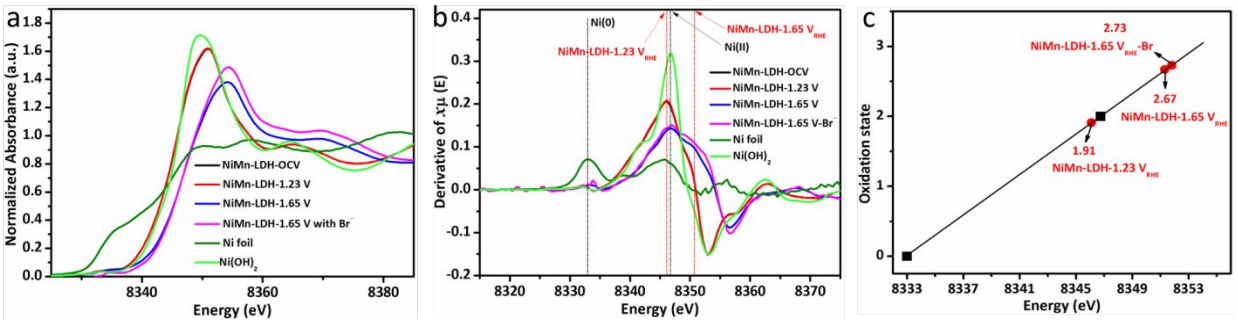

Figure S20. (a) Normalized XANES spectra of Ni K-edge, (b) the first derivative of the normalized XANES spectra of Ni K-edge, and (c) the average oxidation state of Ni ion in NiMn-LDHs obtained from the XANES spectra during the OER process. The *in situ* XANES spectra evidencing that the valence state of Ni ion is less than +3 during the OER process even under high overpotential (1.65 V).

Table S5. Local structure parameters of Ni^{2+} and *in situ* generated Ni^{3+} sites estimated by EXAFS analysis for NiMn-LDHs

	Ni^{2+} phase				Ni^{3+} phase				Summary		
$E_{applied}$	N_{Ni-O}	d_{Ni-O}	N_{Ni-M}	d_{Ni-M}	N_{Ni-O}	d_{Ni-O}	N_{Ni-M}	d_{Ni-M}	R-factor	Total N_{Ni-O}	Total N_{Ni-M}
1.08	4.82±0.43	2.03±0.01	6.00±0.33	3.11±0.01	n/a	n/a	n/a	n/a	0.0014	4.82	6.00
1.23	4.94±0.43	2.03±0.01	6.00±0.32	3.11±0.01	n/a	n/a	n/a	n/a	0.0013	4.94	6.00
1.30	4.93±0.45	2.03±0.01	6.00±0.32	3.11±0.01	n/a	n/a	n/a	n/a	0.0013	4.93	6.00
1.40	4.63±0.56	2.03±0.01	5.08±0.29	3.10±0.01	n/a	n/a	0.92±0.05	2.86±0.03	0.0008	4.63	6.00
1.45	3.31±0.47	2.04±0.11	4.71±0.37	3.10±0.02	1.33±0.37	1.92±0.14	1.29±0.01	2.85±0.03	0.0027	4.64	6.00
1.50	2.50±0.91	2.05±0.04	4.18±0.22	3.10±0.02	1.67±0.64	1.91±0.05	1.82±0.09	2.84±0.02	0.0032	4.18	6.00
1.55	1.90±0.56	2.07±0.06	3.29±0.18	3.10±0.02	2.38±1.15	1.91±0.05	2.71±0.15	2.84±0.02	0.0044	4.28	6.00
1.60	1.05±0.42	2.07±0.07	2.23±0.13	3.11±0.01	2.97±0.86	1.90±0.02	3.77±0.22	2.84±0.01	0.0017	4.02	6.00
1.62	0.76±0.55	2.03±0.09	1.90±0.11	3.10±0.01	2.97±1.04	1.88±0.03	4.10±0.25	2.85±0.01	0.0009	3.73	6.00
1.63	0.34±0.35	2.05±0.12	1.40±1.40	3.09±0.01	3.59±0.61	1.88±0.01	4.60±0.26	2.85±0.01	0.0002	3.93	6.00

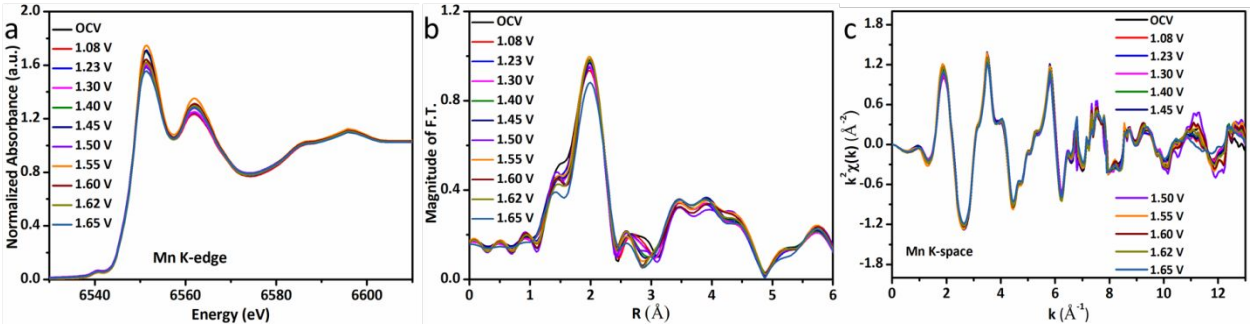

Figure S21. (a) *In situ* XANES spectra (b) Magnitude of *in situ* FT-EXAFS spectra of Mn K-edge for NiMn-LDHs electrocatalyst under the same conditions. (c) *In situ* XANES spectra of extended oscillation functions $k^2\chi(k)$ for Mn K-edge of NiMn-LDHs catalyst.

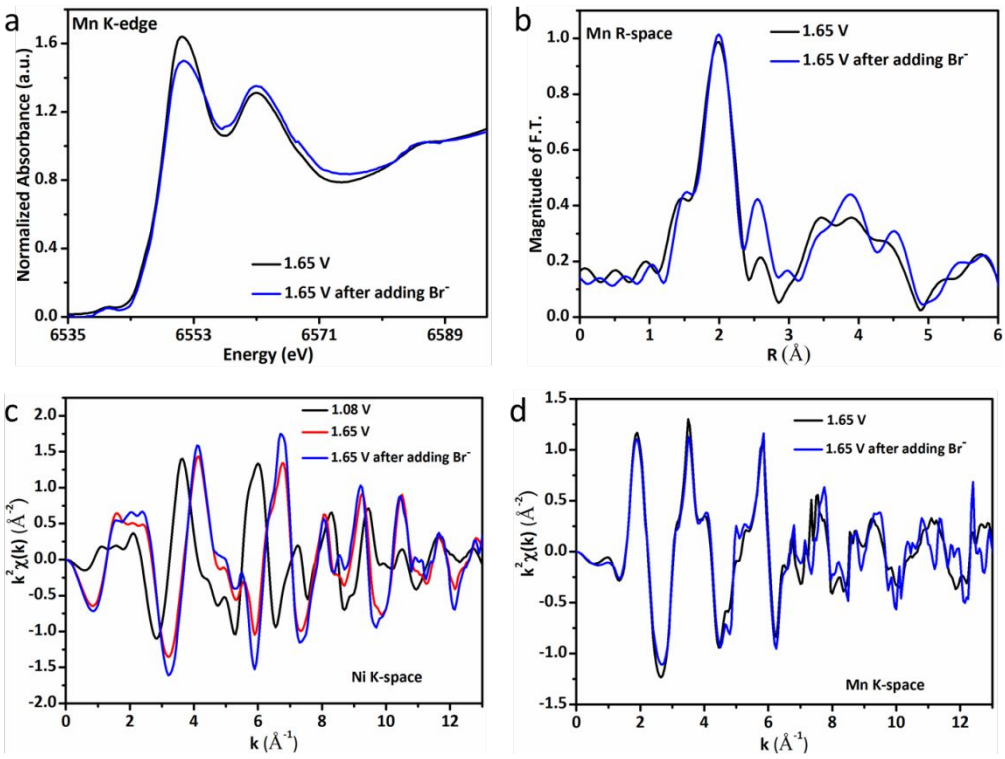

Figure S22. (a) *In situ* XANES (b) Magnitude of FT-EXAFS spectra of Mn K-edge and (c, d) Extended XANES oscillation functions $k^2\chi(k)$ of Ni K-edge and Mn K-edge for NiMn-LDHs before and after bromide guest anion introduced into the electrolyte during the OER.

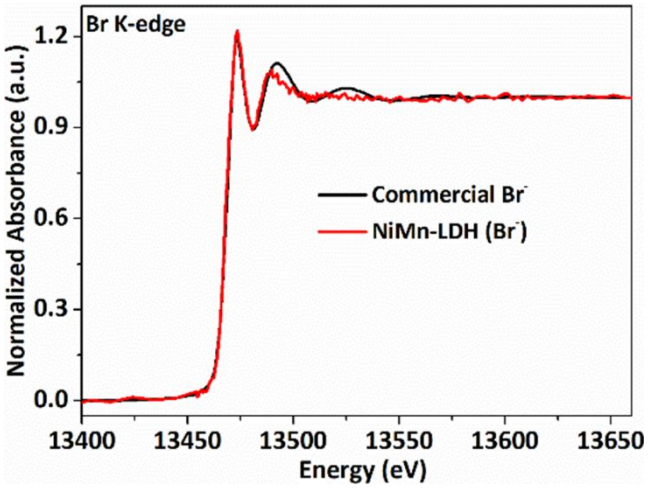

Figure S23. Normalized XANES spectra of Br K-edge for commercial bromide sample and NiMn-LDHs (Br^-) electrode after the OER stability test.

To probe the active site, oxidation state and structural changes of NiMn-LDHs and β-$Ni(OH)_2$ catalysts during the OER, we carried out *in situ* Raman measurements under the same electrochemical conditions (**Figures S24-27**). During the measurements, the working electrode potential was increased in steps from the open-circuit voltage (OCV ~ 1.65 V *vs*. RHE). Each potential was held for at least 15 min until the spectra were recorded. The study of the structural change during the catalytic activity of NiMn-LDHs and β-$Ni(OH)_2$ catalysts and the effect of guest anion lets us know the active sites and better understanding of the site activity and accessible site populations associated with the overall activity.

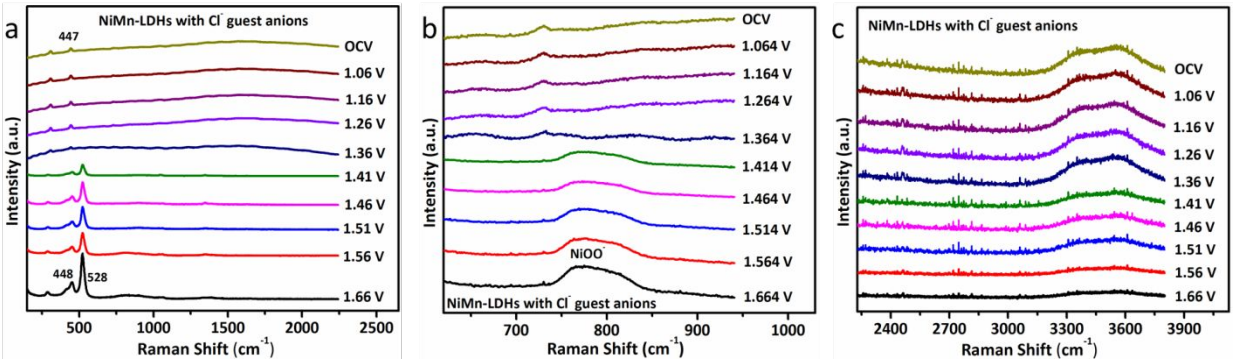

Figure S24. The *in situ* Raman spectra of NiMn-LDHs collected during the OER in the presence of guest anion (13 mM of chloride) in the potential window of 1.064−1.664 V *vs*. RHE in 0.1 M KOH.

The *in situ* Raman spectra of NiMn-LDHs (**Figure S25a**) before a redox transition from 1.064 to 1.364 V display a single peak at 458 cm^{-1}, which is assigned to the stretching modes of Ni–O of $Ni(OH)_2$ species of LDHs.[18] The redox transition of $Ni(OH)_2$/NiOOH of NiMn-LDHs occurs at the potentials higher than 1.364 V (*i.e*., at the anodic wave seen in CV) and the two peaks at 450 and 530 cm^{-1} in the Raman spectra at a potentials higher than 1.364 V attributed to the e_g bending and A_{lg} stretching modes of Ni–O in NiOOH, respectively, which is consistent with the previously

reported literature for NiFe-LDHs.[19, 20] The *in situ* Raman spectra of NiMn-LDHs were also collected at high Raman shifts (2500−3800 cm^{-1}) to see the vibrational stretching modes of O−H during the OER process (**Figure S25b**). The broad band at about 3581cm^{-1} is assigned to O−H vibrations of disordered $Ni(OH)_2$ in NiMn-LDHs. This feature further reveals that introduction of Mn into ordered β-$Ni(OH)_2$ results in structurally disordered LDHs which is beneficial for the enhanced OER activity. This band rapidly weakens and is absent as the electrode potential turns above 1.464 V (*i.e.*, the OER potential range), suggesting that deprotonated NiOOH species. In the case of *in situ* Raman spectra of β-$Ni(OH)_2$, **Figure S27a**, the band at 458 cm^{-1} below 1.364V is attributed to the stretching modes of Ni–O in $Ni(OH)_2$.[21] The pair of peaks observed at 479 and 528 cm^{-1} above the potential of 1.464 V attributed to the bending vibration and stretching modes of Ni–O in NiOOH resulted from the redox transition of $Ni(OH)_2$/NiOOH.[18, 21] The Raman features at 3580 cm^{-1} ascribed to O−H vibrations of $Ni(OH)_2$ (**Figure S27b**) and this peak is absent in the OER potential range above 1.514 V, suggesting deprotonated NiOOH species.

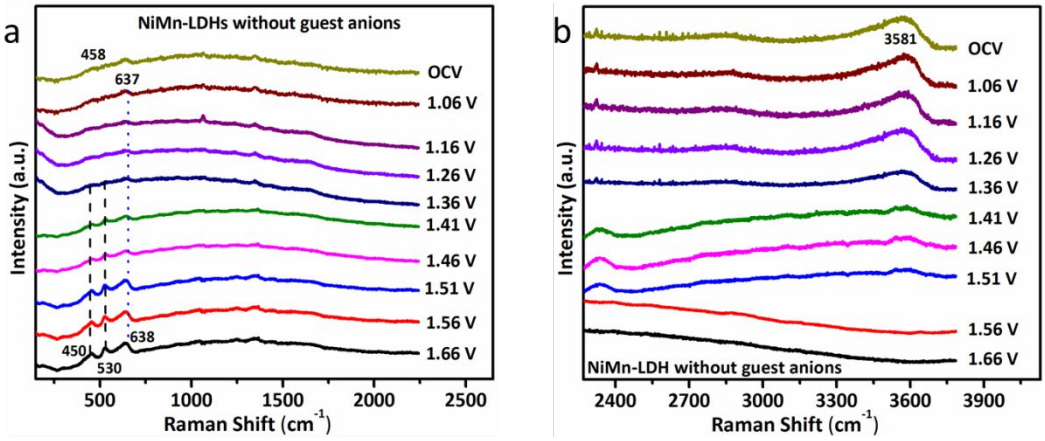

Figure S25. *Operando* Raman spectra of NiMn-LDHs attained in the potential window of 1.064−1.664 V *vs*. RHE in 0.1 M KOH electrolyte. The measurements were conducted chronoamperometrically.

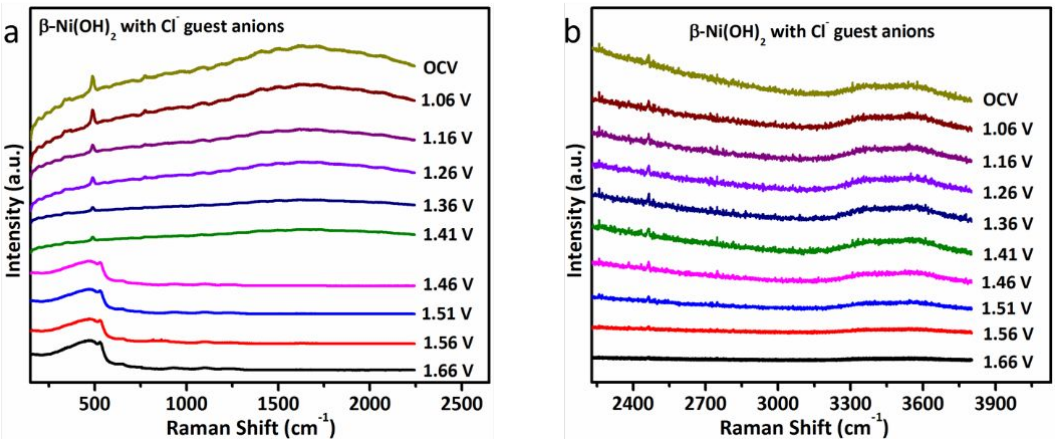

Figure S26. *Operando* Raman spectra of β-Ni(OH)$_2$ collected during the OER in the presence of guest anion (13 mM of chloride) in 0.1 M KOH.

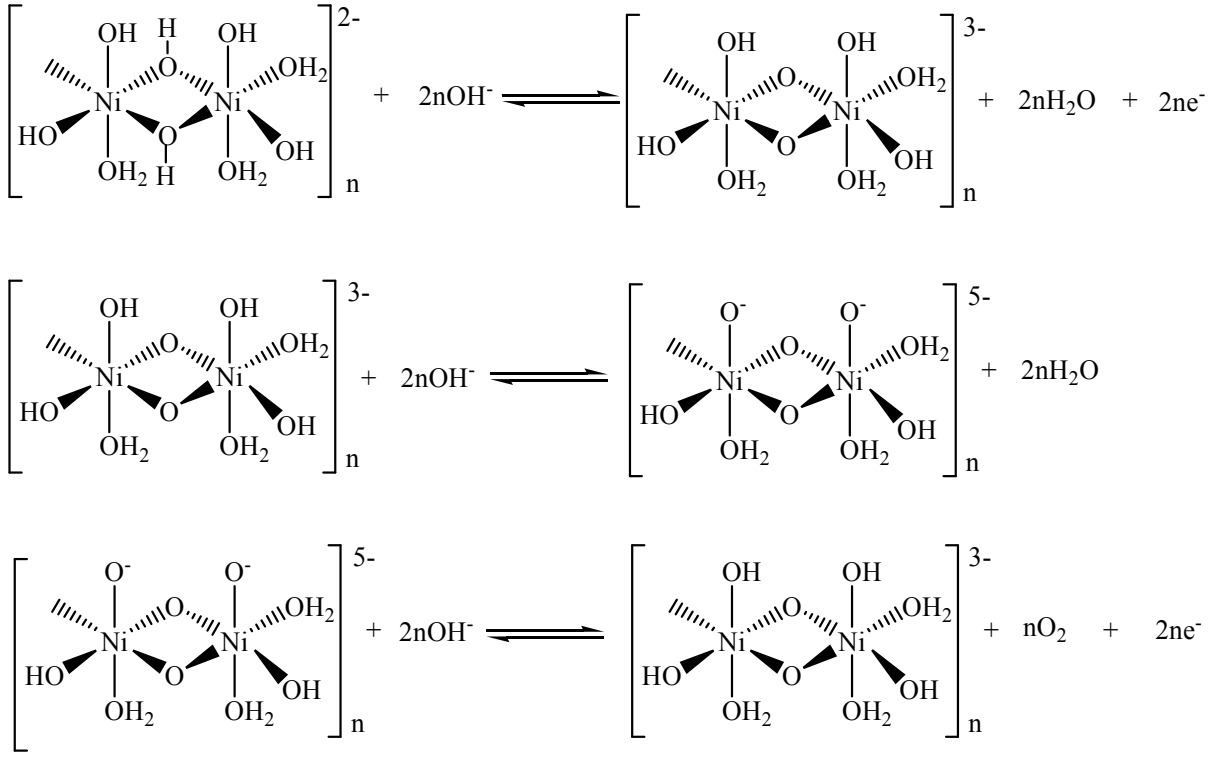

Scheme S1. The hypothesized OER mechanism on NiMn-LDHs catalyst was suggested by the *operando* XAS and *operando* Raman measurements.

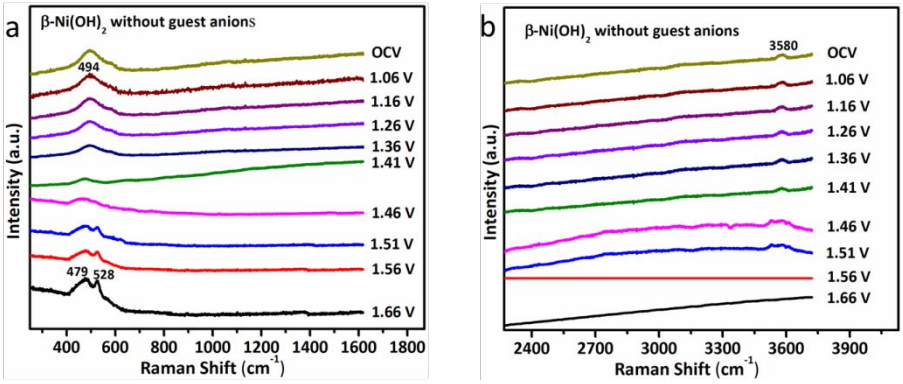

Figure S27. *Operando* Raman spectra of synthesized ordered β-$Ni(OH)_2$ attained in the potential window of 1.064−1.664 V *vs.* RHE in 0.1 M KOH electrolyte.

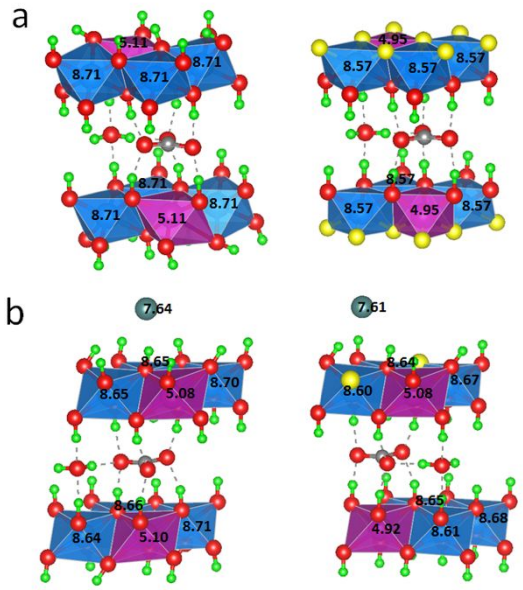

Figure S28. Bader charge analysis for NiMn-LDH(CO_3) without/with intercalation of guest anion Br. The values nearby different atoms represent Bader charge. (a) NiMn-LDH(CO_3), left: $Ni(OH)_2$ structure, and right: NiOOH structure. (b) NiMn-LDH(CO_3) with intercalation of guest anion Br, left: $Ni(OH)_2$ structure and right: one NiOOH site (yellow ball). Blue, purple, grey, red, green, and cyan balls represent Ni, Mn, carbon, oxygen, hydrogen, and Br, respectively.

To verify the interaction between the two metals after hybridization, the partial electron transfer process from Ni to Mn through the oxygen ligand is explained in terms of their electronic configuration as shown in **Figure S29**. The valence state of Ni^{2+} electronic configuration is $3d^8$ and exhibits the high spin state of octahedral geometry. Thus, the t_2g (π-symmetry d-orbitals) of $3d^8$ octahedral geometry of Ni^{2+} is fully occupied. As such, the major electronic interaction between the bridging and Ni^{2+} is e^-–e^- repulsion. Similarly, the valence state of Mn^{3+} electronic configuration is $3d^4$ and exhibits high spin octahedral geometry with an unpaired electron in the π-symmetry of t_2g orbitals. Hence, Mn^{3+} interacts with the bridging O^{2-} *via* π-donation. We, therefore, claim that the π-donation of Mn−O can be intensified by the e^-–e^- repulsion between Ni^{2+} and O^{2-}, which generates the partial charge transfer between Mn and Ni. This can indicate that the coupling between the Ni and Mn could induce a change in electronic and conductivity properties which in turn improves the OER activity. The spectro-electrochemical experiments have further verified the advantage of the coupling effect between Ni and Mn, which accounts for the improved OER activity of NiMn-LDHs compared with β-$Ni(OH)_2$.

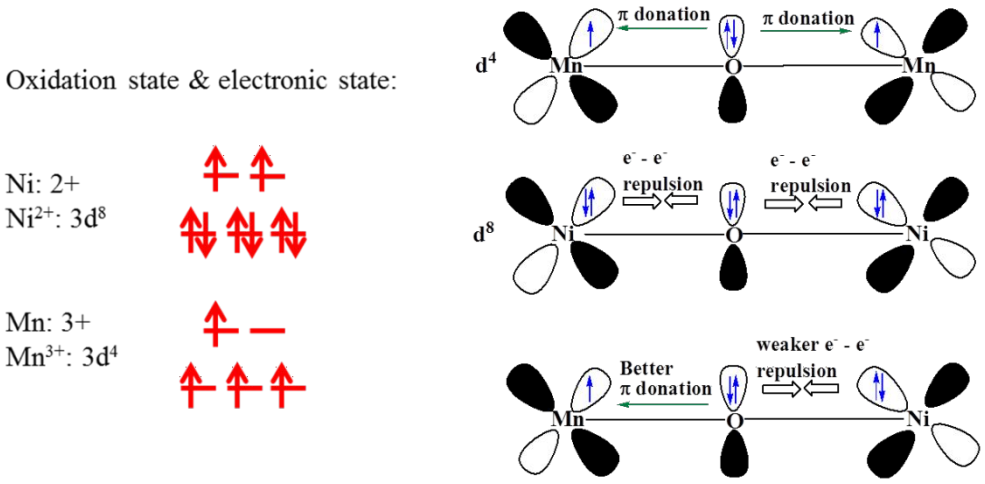

Figure S29. The schematic representation of the electronic coupling between Ni and Mn species in NiMn-LDHs.

References

1. Hwang, B. J.; Senthil Kumar, S. M.; Chen, C.-H.; Chang, R.-W.; Liu, D.-G.; Lee, J.-F., Size and Alloying Extent Dependent Physiochemical Properties of Pt−Ag/C Nanoparticles Synthesized by the Ethylene Glycol Method. *J. Phys. Chem. C* **2008,** *112*, 2370-2377.
2. Kresse, G.; Hafner, J., *Ab Initio* Molecular Dynamics for Liquid Metals. *Phys. Rev. B* **1993,** *47*, 558-561.
3. Perdew, J.; Burke, K.; Ernzerhof, M., of Physics, D.; Quantum Theory Group Tulane University, NOL 70118. *J. Phys. Rev. Lett.* **1996,** *77*, 3865-3868.
4. Kresse, G.; Joubert, D., From Ultrasoft Pseudopotentials to the Projector Augmented-Wave Method. *Phys. Rev. B* **1999,** *59*, 1758.
5. Grimme, S.; Antony, J.; Ehrlich, S.; Krieg, H., A Consistent and Accurate *ab Initio* Parametrization of Density Functional Dispersion Correction (DFT-D) for the 94 Elements H-Pu. *J. Chem. Phys.* **2010,** *132*, 154104.
6. Grimme, S.; Ehrlich, S.; Goerigk, L., Effect of the Damping Function in Dispersion Corrected Density Functional Theory. *J. Comput. Chem.* **2011,** *32*, 1456-1465.
7. Chala, S. A.; Tsai, M.-C.; Su, W.-N.; Ibrahim, K. B.; Duma, A. D.; Yeh, M.-H.; Wen, C.-Y.; Yu, C.-H.; Chan, T.-S.; Dai, H.; Hwang, B.-J., Site Activity and Population Engineering of NiRu-Layered Double Hydroxide Nanosheets Decorated with Silver Nanoparticles for Oxygen Evolution and Reduction Reactions. *ACS Catal.* **2019,** *9*, 117-129.
8. Gong, M.; Li, Y.; Wang, H.; Liang, Y.; Wu, J. Z.; Zhou, J.; Wang, J.; Regier, T.; Wei, F.; Dai, H., An Advanced Ni–Fe Layered Double Hydroxide Electrocatalyst for Water Oxidation. *J. Am. Chem. Soc.* **2013,** *135*, 8452-8455.
9. Chala, S. A.; Tsai, M.-C.; Su, W.-N.; Dai, H.; Hwang, B. J., *Layered Double Hydroxide Nanosheets Decorated with Metal or Metal Oxides for Oxygen Evolution and Reduction Reactions*, Abstracts of Papers of the American Chemical Society, *Am. Chem. Soc.* 1155 16th St, NW, Washington, DC 20036 USA: 2019.
10. Fan, K.; Chen, H.; Ji, Y.; Huang, H.; Claesson, P. M.; Daniel, Q.; Philippe, B.; Rensmo, H.; Li, F.; Luo, Y.; Sun, L., Nickel–Vanadium Monolayer Double Hydroxide for Efficient Electrochemical Water Oxidation. *Nat. Commun.* **2016,** *7*, 11981.
11. Chala, S. A.; Tsai, M.-C.; Su, W.-N.; Ibrahim, K. B.; Thirumalraj, B.; Chan, T.-S.; Lee, J.-F.; Dai, H.; Hwang, B.-J., Hierarchical 3D Architectured Ag Nanowires Shelled with NiMn-Layered Double Hydroxide as an Efficient Bifunctional Oxygen Electrocatalyst. *ACS Nano* **2020,** *14*, 1770-1782.
12. Zhang, J.; Liu, J.; Xi, L.; Yu, Y.; Chen, N.; Sun, S.; Wang, W.; Lange, K. M.; Zhang, B., Single-Atom Au/NiFe Layered Double Hydroxide Electrocatalyst: Probing the Origin of Activity for Oxygen Evolution Reaction. *J. Am. Chem. Soc.* **2018,** *140*, 3876-3879.
13. Zhou, D.; Cai, Z.; Lei, X.; Tian, W.; Bi, Y.; Jia, Y.; Han, N.; Gao, T.; Zhang, Q.; Kuang, Y.; Pan, J.; Sun, X.; Duan, X., NiCoFe-Layered Double Hydroxides/N-Doped Graphene Oxide Array Colloid Composite as an Efficient Bifunctional Catalyst for Oxygen Electrocatalytic Reactions. *Adv. Energy Mater.* **2018,** *8*, 1701905.
14. Zhao, S.; Wang, Y.; Dong, J.; He, C.-T.; Yin, H.; An, P.; Zhao, K.; Zhang, X.; Gao, C.; Zhang, L.; Lv, J.; Wang, J.; Zhang, J.; Khattak, A. M.; Khan, N. A.; Wei, Z.; Zhang, J.; Liu, S.; Zhao, H.; Tang, Z., Ultrathin Metal–Organic Framework Nanosheets for Electrocatalytic Oxygen Evolution. *Nat. Energy* **2016,** *1*, 16184.

15. Wang, Y.; Zhang, Y.; Liu, Z.; Xie, C.; Feng, S.; Liu, D.; Shao, M.; Wang, S., Layered Double Hydroxide Nanosheets with Multiple Vacancies Obtained by Dry Exfoliation as Highly Efficient Oxygen Evolution Electrocatalysts. *Angew. Chem., Int. Ed.* **2017,** *56*, 5867-5871.
16. Liu, R.; Wang, Y.; Liu, D.; Zou, Y.; Wang, S., Water-Plasma-Enabled Exfoliation of Ultrathin Layered Double Hydroxide Nanosheets with Multivacancies for Water Oxidation. *Adv. Mater.* **2017,** *29*, 1701546.
17. Li, C.; Zhang, Z.; Liu, R., *In Situ* Growth of 3D NiFe LDH-POM Micro-Flowers on Nickel Foam for Overall Water Splitting. *Small* **2020,** *16*, 2003777.
18. Lo, Y. L.; Hwang, B. J., *In Situ* Raman Studies on Cathodically Deposited Nickel Hydroxide Films and Electroless Ni−P Electrodes in 1 M KOH Solution. *Langmuir* **1998,** *14*, 944-950.
19. Diaz-Morales, O.; Raaijman, S.; Kortlever, R.; Kooyman, P. J.; Wezendonk, T.; Gascon, J.; Fu, W. T.; Koper, M. T. M., Iridium-Based Double Perovskites for Efficient Water Oxidation in Acid Media. *Nat. Commun.* **2016,** *7*, 12363.
20. Yang, L.; Liu, D.; Hao, S.; Kong, R.; Asiri, A. M.; Zhang, C.; Sun, X., A Cobalt-Borate Nanosheet Array: An Efficient and Durable Non-Noble-Metal Electrocatalyst for Water Oxidation at near Neutral pH. *J. Mater. Chem. A* **2017,** *5*, 7305-7308.
21. Trześniewski, B. J.; Diaz-Morales, O.; Vermaas, D. A.; Longo, A.; Bras, W.; Koper, M. T. M.; Smith, W. A., *In Situ* Observation of Active Oxygen Species in Fe-Containing Ni-Based Oxygen Evolution Catalysts: The Effect of pH on Electrochemical Activity. *J. Am. Chem. Soc.* **2015,** *137*, 15112-15121.